







Generation of extreme-ultraviolet and x-ray light from a propagating nanometer electron layer in few-cycle laser interaction with solid targets

Xinmeng Liu ¹, Dongning Yue ^{1,2,*}, Quanli Dong ^{1,2,†}, Ziqiang Shao ¹, Zhe Li,¹ Hao Teng,³ Zhiyi Wei,³ Feng Liu ^{4,2},
Boyuan Li,^{4,2} Xiaohui Yuan,^{4,2} Min Chen ^{4,2}, Zhengming Sheng ^{4,2} and Jie Zhang^{4,2}

¹*School of Physics, Harbin Institute of Technology, Harbin 150001, China*

²*Collaborative Innovation Center of IFSA (CICIFSA), Shanghai Jiao Tong University, Shanghai 200240, China*

³*Beijing National Laboratory for Condensed Matter Physics, Institute of Physics, Chinese Academy of Sciences, Beijing 100190, China*

⁴*Key Laboratory for Laser Plasmas (Ministry of Education), School of Physics and Astronomy, Shanghai Jiao Tong University, Shanghai 200240, China*



(Received 5 February 2024; accepted 25 March 2024; published 18 April 2024)

A new generation mechanism of coherent extreme-ultraviolet (XUV) and x-ray radiation presents in the few-cycle laser interaction with solid density plasma. Two-dimensional simulations show that the XUV and x-rays intensities do not have power law or exponential law dependence on the frequency which is followed by the high harmonic spikes generated through the coherent-wake-emission or relativistically oscillating mirror processes. The XUV and x rays are actually nonlinearly scattered by the successively propagating nanometer electron layers formed in the combined effects of the ponderomotive forces of the incident laser pulse and the electric force due to the charge separation. The nanometer electron layers move in the laser field and the characteristic electrons have their directions bended several times due to the change of the laser's magnetic field. At every bending point, these electrons emit strong synchrotron radiation along a direction that deviates from the reflected laser, even if the normalized drive laser amplitude is at $a_0 \approx 1$. The simulation results for two cases with and without the density profile truncation indicate that the efficiency of this mechanism strongly depends on the preplasma.

DOI: [10.1103/PhysRevA.109.043519](https://doi.org/10.1103/PhysRevA.109.043519)

I. INTRODUCTION

Bright coherent extreme-ultraviolet (XUV) and x rays are important light sources for applications in the diagnosis of atomic and molecular dynamics [1], free-electron lasers [2], and coherent diffraction imaging [3]. For the generation of XUV and x rays, one promising method is utilizing ultraintense laser pulse irradiating a solid target to generate high-order harmonics (HHG) which inherits the full temporal and spatial coherence, as well as the perfect temporal synchronization. This method also has advantages over experiments with gas targets since there are no limits on the applicable laser intensity by the ionization processes [4–6] and the frequency-up-conversion efficiency increases along with the laser intensity so that scientific research on ultrashort x-ray nonlinear optics becomes achievable [7–9]. Three main mechanisms of HHG in laser interaction with solid targets have been identified both experimentally and theoretically, i.e., coherent wake emission (CWE) [10,11], the relativistically oscillating mirror (ROM) [12,13], and coherent synchrotron emission (CSE) by electron bunches [14,15]. The efficiency and quality of HHG rely on laser and plasma parameters, such as the laser pulse intensity, polarization, and temporal profile contrast [16–18]; the target shape or structure [19–24]; the preplasma scale length [25–29]; the angle of

incidence [30,31], etc. With the development of few-cycle lasers and their applications in the generation of XUV and x-ray pulses [32–36], it is possible to examine the HHG mechanism through the radiation property measurements by getting rid of the interference effects usually existing in multicycle long-laser-pulse experiments. With the interaction mechanism being deeply understood, one can investigate the effects of the carrier envelope phase (CEP) on HHG and produce experimentally the single attosecond pulse that is necessary to put the pump-probe technique into applications in ultrafast physical process detection [37]. With applications of ultraintense few-cycle laser pulses in HHG experiments, it is largely possible that the CSE from relativistic electron nanobunches will take place on the microscopic level when proper physical conditions are matched [15]. Such processes were discovered by van der Brugge and Pokhov and then further investigated by others [38–41], usually with one-dimensional particle-in-cell (1D PIC) simulations. However, two-dimensional physical effects still need to be considered, especially in situations with oblique incident laser pulses and different plasma density profiles.

In this paper, we report results of two-dimensional PIC simulations about the generation of XUV and x rays in a few-cycle laser pulse interaction with solid targets. It is found that the XUV and x-ray intensities do not follow power law or exponential law as usually found for the CWE and ROM mechanism reported in previous papers [41–43]. In particular, two XUV and x-ray radiation bands are found isolated from the background lower-frequency harmonics spectrum, and

*ydn@hit.edu.cn

†qldong@aphy.iphy.ac.cn

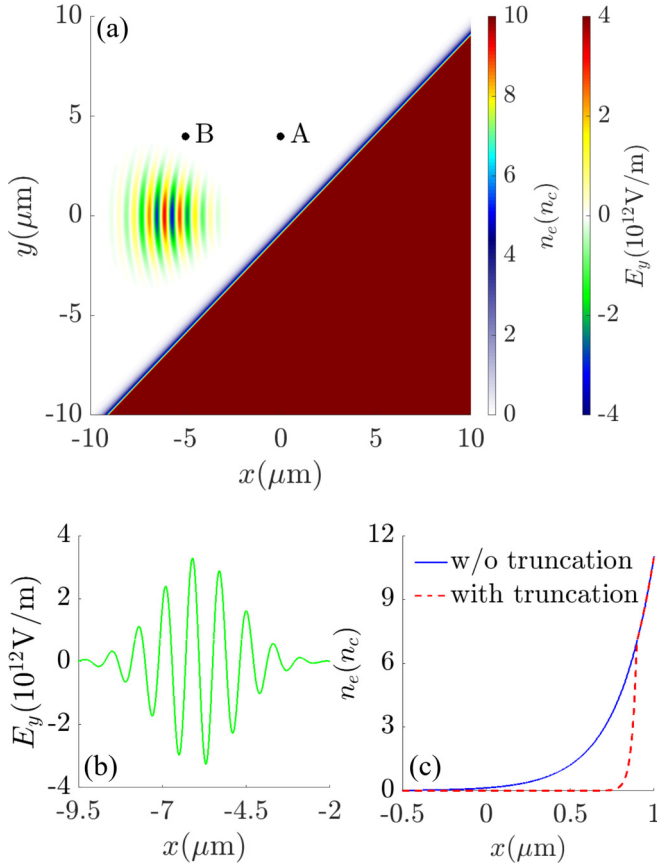


FIG. 1. (a) The setup of the initial laser-plasma conditions with different preplasma ramp shapes. The incident laser beam radiates on the target front surface with an incidence angle $\alpha = 45^\circ$. (b) The distribution of the laser electric field E_y at the initial moment. (c) Two different kinds of preplasma density profiles on the laser axis. The solid blue line represents without (w/o) the density profile truncation, and the dashed red line represents with the profile truncation.

their radiation directions deviate from the laser reflection direction. This cannot be explained with the models mentioned above. In this work, we show that the generation of XUV and x rays depends on nanometer electron layers formed by the combination effects of the ponderomotive force of the laser pulse and the electrostatic field induced by charge separation.

II. SIMULATION PARAMETER SETUP

The two-dimensional PIC code OSIRIS [44] was used to study the generation of XUV and x rays. The schematic of laser plasma parameters is shown in Fig. 1(a). The intensity of the incident laser pulse is normalized by $a_0 = eE_y/m_e\omega_0c$ and $a_0 = 1.0$, where e and m_e are the charge and mass of a single electron, respectively, E_y is the initial laser electric field, ω_0 is the angular frequency of the laser pulse. The laser pulse has a Gaussian profile in both longitudinal and transverse directions. The laser wavelength and period are $\lambda_0 = 800$ nm and $T_0 = \lambda_0/c$, where c is the light speed in vacuum. The laser beam full-width-at-half-maximum focus diameter is 2.0 μm at $x = 0.0$ μm and the pulse duration is $\tau = 3.0 T_0 = 8$ fs which makes it a few-cycle pulse as shown in Fig. 1(b). The laser pulse is incident from the left boundary of the simulation

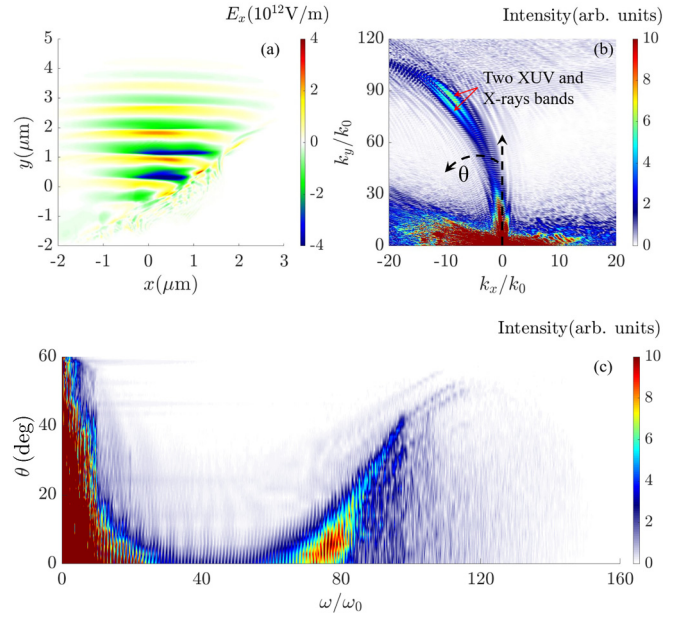


FIG. 2. Distributions of the reflected laser electric field E_x in (a) spatial space (x, y) and (b) the corresponding wave vector space (k_x, k_y) in units of k_0 , where k_0 is the wave vector of the incident laser pulse, at $t = 10.0T_0$ without (w/o) truncation. Two radiation bands whose frequencies are cross extreme ultraviolet (XUV) and x-ray wave bands are found in panel (b). (c) The angular distribution of the spectra in units of degrees. The θ direction is shown in panel (b), where $\theta = 0^\circ$ is the normal laser reflection direction.

box with an incidence angle $\alpha = 45^\circ$. The solid target has a maximum density with $n_{\text{max}} = 100.0n_c$, where n_c is the critical density for λ_0 and an exponentially increasing preplasma density with a scale length of $L = 0.16$ μm . The preplasma density gradient is perpendicular to the solid target surface. For comparison, two different kinds of preplasma density profiles have been taken in our simulations as given in Fig. 1(c), i.e., with and without truncation. The simulation box range is -10 $\mu\text{m} \leq x \leq 10$ μm and -10 $\mu\text{m} \leq y \leq 10$ μm . The box is divided into 8000×8000 cells totally, which can provide a resolution of 2.5 nm. We set 16 electrons (macroparticles) and immobile ions in each cell.

III. SPECTRAL PROPERTIES OF THE HIGH HARMONICS

We analyze the frequency of the reflected laser pulse passing through points A and B, with A located in the right reflection direction. Figure 2 shows the electric field E_x and the corresponding spectra of reflected laser pulses and their angular distribution, which indicates two radiation bands with frequency located within the XUV and x-ray ranges [see Fig. 2(b)]. The angular distribution of the spectra as given in Fig. 2(c) shows that the XUV and x rays deviate from the laser reflection. The maximum angle could reach about 40° . It is little possible for such angular deviation to be introduced by the numerical dispersion [45]. To further examine the angular distribution, we perform a more refined simulation with the same laser-plasma parameters which only doubles the spatial resolution since it can significantly reduce the numerical angular deviation. The results show almost the same XUV and

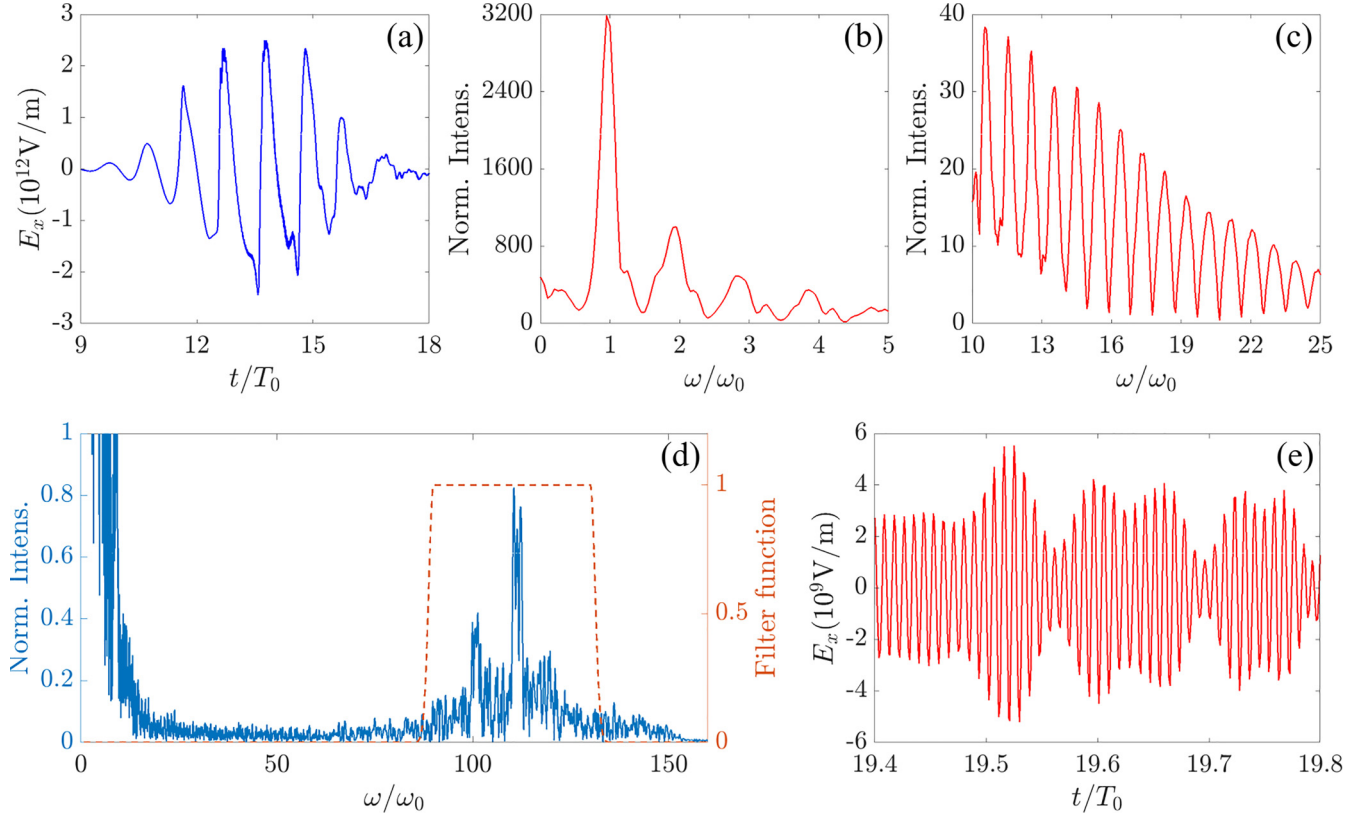


FIG. 3. Distributions of (a) the reflected laser electric field E_x and (b, c) the corresponding frequency spectra in units of laser frequency ω_0 at point A in Fig. 1(a) without truncation. The orders are from (b) 1st to 4th and (c) 11th to 25th. The frequency spectra are with the normalized intensity (i.e., Norm. Intens.). (d) The frequency spectrum (the solid blue line) with the x-ray wave band and (e) the corresponding inverse fast Fourier transformation (iFFT) after filtering [the dashed orange line in panel (d)] at point B in Fig. 1(a) without truncation.

x-ray bands, so we can eliminate the effects of the numerical dispersion. The temporal distribution and corresponding frequencies of the electric field E_x at point A are given in Figs. 3(a)–3(c). From the scaling law of the high harmonic (HH) intensity versus orders, it is found that the HHG can be attributed to two mechanisms, the CWE in orders from $n = 1$ st to 4th in Fig. 3(b) and the ROM in orders from $n = 10$ th to 25th in Fig. 3(c). Both of their spectral strengths scale with orders in a power law. The HHG order is limited to $n = 60$ th, at which frequency the radiation intensity becomes very weak. To find the position dependence of the HH property, Fig. 3(d) gives the spectra recorded at point B, showing that HH orders between $n = 100$ th and $n = 110$ th are also produced [46–48].

IV. DYNAMICS OF ELECTRONS EMITTING THE HIGH HARMONICS

To find out the mechanism for the generation of XUV and x rays, we record the temporal evolution of the preplasma density profile since the incident laser pulse is as given in Fig. 4. The electrons pile up and form an electron layer by the ponderomotive force of the laser pulse at different preplasma areas. The incident laser pulse intensity I can be expressed as $I = I_0 \exp(-r^2/R_L^2) \exp[-(x - x_{\text{cent}})^2/(c^2 T_L^2)]$, where $I_0 = 1.37 \times 10^{18} a_0^2/\lambda_0^2 [\mu\text{m}] \text{ W/cm}^2$, x_{cent} is the position of the laser pulse center, $R_L = 1.2 \mu\text{m}$ is the $1/e^2$ focus radius, and

$T_L = \tau/2\sqrt{\ln 2}$. The longitudinal and radial ponderomotive forces, f_x and f_r , have the forms of $f_x \propto -\partial I/\partial x$ and $f_r \propto -\partial I/\partial r$. So, f_x and f_r get their maximum values $f_{x\text{max}}$ and $f_{r\text{max}}$ at $|x - x_{\text{cent}}| = cT_L/\sqrt{2}$ and $r = R_L/\sqrt{2}$, respectively.

The original electron layer forms in the balance of the ponderomotive force f_r with the charge separation electric field E_f in the radial direction macroscopically. The radial ponderomotive force f_r has the expression $f_r = -\frac{e^2}{4m_e\omega_0^2\epsilon_0 c} \frac{\partial I}{\partial r} [1 - \cos(2\omega_0 t)]$. With the $[1 - \cos(2\omega_0 t)]$ term ignored, we have $f_r \sim 10^{-9} \text{ N}$ around the laser focus. It is approximated that $E_f e(n_{\text{peak}} - n_0)d_s/2 \approx (n_{\text{peak}} - n_0) \int_{r_a}^{r_b} f_r dr$, where n_{peak} and n_0 are the peak and the original electron density of the electron layer, d_s is the original thickness of the electron layer, and $|r_b - r_a| \sim L$ is the radial interaction distance of the incident laser and the preplasma around the critical-density plane. According to the simulation results, one has the following analytical estimates, $E_f \sim 10^{11} \text{ V/m}$, $\int_{r_a}^{r_b} f_r dr \sim 10^{-16} \text{ N m}$, and $d_s \sim 10 \text{ nm}$, which are consistent with the simulation results.

The nanometer electron layers are modulated by both the incident and the reflected laser pulses, so that they are not stable. The thin layer is embedded within the laser electromagnetic fields and the charge separation electric field E_f , as shown in Figs. 5(c) and 5(d). At the beginning of formation, the two side surfaces of the thin layer are subjected to electric forces with opposite directions, and the electron layer splits.

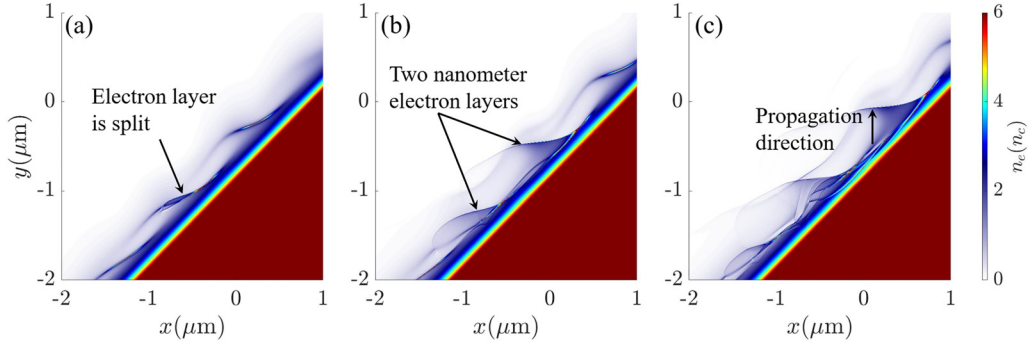


FIG. 4. The temporal evolution of the electron density n_e at (a) $t = 6.25T_0$, (b) $t = 7.0T_0$, and (c) $t = 7.5T_0$.

One is dragged into the inner plasma area and the other moves along the plasma surface stably. As one can see from Figs. 4(a) and 4(b), two nanometer electron layers of high density and smaller thickness are formed by E_f and f_r at $t = 6.25T_0$. Both of them move along the $+y$ direction as shown in Figs. 4(b) and 4(c), although they deviate from this direction a little. Within a few laser periods, the two nanometer electron layers can be maintained, and they keep their profiles and behave like solitary waves during their propagating process. The moving velocity of the nanometer electron layer is about $0.9c$.

In the longitudinal direction, the electron layer can hardly get split because the radiation pressure $\sqrt{2}I/c$ can hold the electron layer as a whole. So the split of the electron layer happens on the edge of the radial laser focus since the laser intensity is weak and the laser gets reflected quickly in this area.

Characteristic electrons emitting HH around the 100th order show similar moving tracks and motion patterns. A typical

electron track is shown in Fig. 6(a) with the background of electron density. Comoving within the nanometer layer, the single electron also runs along the $+y$ direction due to combination effects of the charge separation electric field E_f and the laser electric field after its first oscillation at the original position when the incident laser pulse comes. After the electron layer split, the moving nanometer electron layers elongate along the x direction due to the stretch of E_f and the laser electric field E_x . This is because the ponderomotive pressure of the laser pulse keeps compressing the electron layer along the direction perpendicular to the gradient of the preplasma density as shown in Figs. 4(b) and 4(c). The nanometer electron layers also get thinner along the $-x$ direction and can get as thin as ~ 7.0 nm. The whole nanometer structure is in the laser magnetic field B_z . With the nanometer electron layer moving, the single electron undergoes a gradual deceleration because it moves slower than the phase velocity of the nanometer electron layer. Once the single electron falls behind of the nanometer electron layer, the charge separation electric field E_f makes the single electron decelerate further. When the single electron is decelerated to a velocity $v \sim 0.1c$, the single electron begins to turn back at point 1 as shown in Figs. 6(a) and 6(c). This is caused by the Lorentz force of the laser magnetic field B_z when $B_z > 0$. With the single electron turning back, it emits synchrotron radiation at point 1 when it is bent by the magnetic field. After passing point 1, the single electron moves toward the overdense plasma and feels that the laser magnetic field B_z changes its direction rapidly, i.e., $B_z < 0$, as the reflected laser propagates. Then, the single electron turns to the left because the direction of the Lorentz force gets reversed. Then, the direction of B_z changes to $B_z > 0$ again and the single electron turns back at point 2 as shown in Figs. 6(a) and 6(c). At point 2, the single electron also emits synchrotron radiation for the second time. However, the intensity of this second emission should be very weak since the electron density is low and the kinetic energy is small. After that, the single electron is dragged into the solid-plasma area by the charge separation electric field. One can evaluate the radiant power of the synchrotron P_s by using $P_s = n_e e^4 v^2 B_z^2 / 16\pi^2 \epsilon_0 m_e^2 c^3$, or the radiation intensity relies on the electron density n_e and its kinetic energy. As one can see from Fig. 6(b), the density of the nanometer electron layer can reach as high as $3n_c$. If we take $v \sim 0.1c$ and $B_z \sim 10^3 T$, we can estimate that $P_s \sim 10^{11}$ W/cm², which is the same amplitude from simulations. There are two nanometer electron layers moving along the $+y$ direction as shown in Fig. 4(b) and they

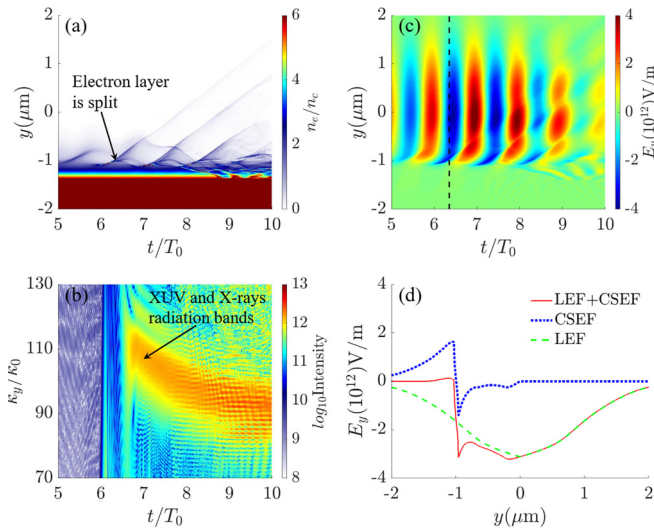


FIG. 5. The temporal evolution of (a) the electron density n_e , (b) the logarithmic wave vector intensity, and (c) the laser electric field E_y (the charge separation electric field is also overlaid on this colormap) on the $x = -0.5 \mu\text{m}$ line. (d) The distribution of the laser electric field (LEF, the dashed green line), the charge separation electric field (CSEF, the dotted blue line), and their summing field (LEF + CSEF, the solid red line) at $t = 6.35T_0$ [i.e., the dashed black line in panel (c)].

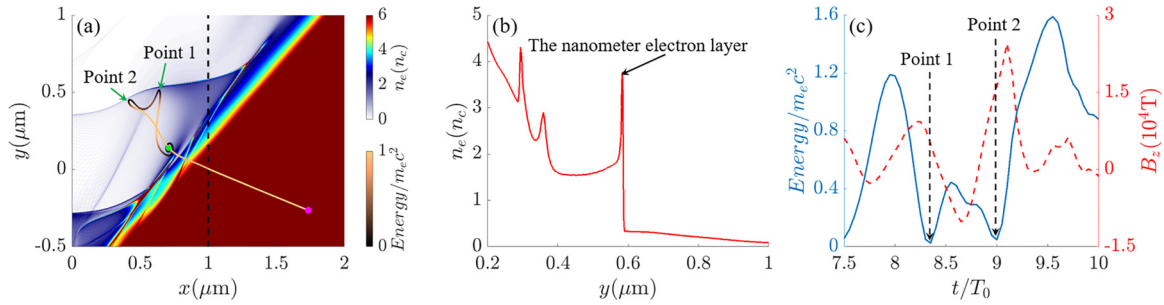


FIG. 6. (a) Typical trajectory of electron motion in laser preplasma interaction without truncation. The green point represents the initial position of the selected electron while the magenta point represents its final position (the same below). The color of the trajectory represents the electron's kinetic energy (the same below). The background color shows the distribution of the electron density n_e at $t = 8.25T_0$. (b) The distribution of the electron density n_e at $x = 1.0 \mu\text{m}$ [the dashed black line in panel (a)]. (c) The energy of the selected electron (the solid blue line) and the magnetic field B_z (the dashed red line) that the electron experiences.

emit two corresponding XUV and x-ray bands, producing the interference-fringe-like structures as shown in Fig. 5(b).

The preplasma is important for the electron layer formation and the HHG through the CSE mechanism. We also carried out studies with the density profile truncation in the preplasma. The simulation results are shown in Figs. 7–9 for comparison. The HHG generated by the CWE mechanism (orders from $n = 1\text{st}$ to $n = 4\text{th}$) is observed in Figs. 8(a) and 8(b). No HHG generated by the ROM mechanism is observed in this case since the electrons can hardly be accelerated to relativistic velocity because the electron density of $7.0n_c$ at the truncation point is so high that the ponderomotive force can hardly push the electron away from its original position, let alone the formation of large amplitude oscillation and kinetic energy. For the same reason, the maximum order of HHG is limited in this case. One can see from Fig. 8(c), the maximum order is near $n = 20\text{th}$. However, the temporal frequency spectrum shows an isolated frequency from the background at near $n = 20\text{th}$. Its radiation intensity can reach $\sim 10^{11} \text{ W/cm}^2$ as calculated from Fig. 8(d). To find out the origin of the isolated frequency component, we analyze the electrons' motions and the electron density as given in Fig. 9. The $0.01\text{-}\mu\text{m}$ electron layer compressed by the ponderomotive force of the laser pulse is observed and its density can reach as high as $16.0n_c$ from Fig. 9(b). A typical electron track is shown in Fig. 9(a). This electron turns its direction to the

solid-plasma area at point 3 of Fig. 9(a). At the turn point, the electron emits synchrotron radiation. Although the electron layer has a higher electron density, it has kinetic energy lower than that of the case without the density profile truncation and soon collapses into the solid plasma. So the radiation intensity does not improve obviously in this case.

V. CONCLUSION AND DISCUSSION

We show research about few-cycle laser pulse interaction with solid-plasma generating XUV and x rays. The XUV and x-ray intensities do not match the power law or exponential law and their directions deviate from the laser reflection. Further studies show that the XUV and x rays are formed when the laser pulse nonlinearly scattered from propagating nanometer electron layers, whose formation is attributed to the combination effects of the laser ponderomotive force and the electric force due to the charge separation. After the instability and splitting at the formation beginning, the nanometer electron layer propagated along the target surface

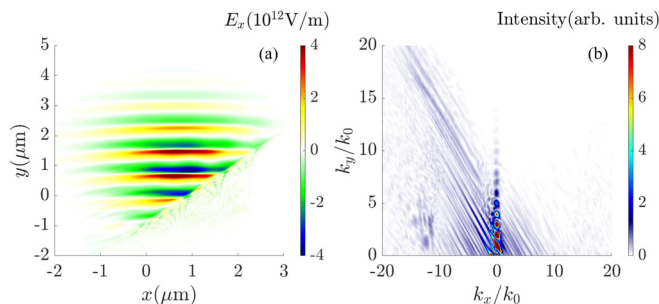


FIG. 7. Distributions of the reflected laser electric field E_x in (a) spatial space (x, y) and (b) the corresponding wave vector space (k_x, k_y) in units of k_0 , where k_0 is the wave vector of the incident laser pulse, at $t = 10.0T_0$ with truncation.

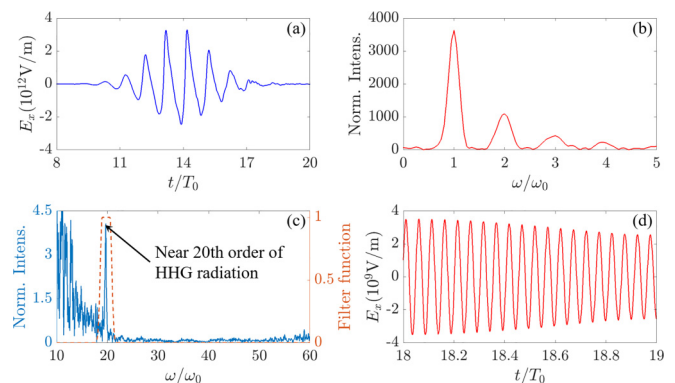


FIG. 8. Distributions of (a) the reflected laser electric field E_x and (b, c) the corresponding frequency spectra in units of laser frequency ω_0 at point A in Fig. 1(a) with truncation. The orders are from (b) 1st to 4th and from (c) 10th to 60th (the solid blue line). The frequency spectra are with the normalized intensity (i.e., Norm. Intens.). (d) The corresponding inverse fast Fourier transformation (iFFT) of the frequency spectrum with near the 20th order after filtering (the dashed orange line) at point B in Fig. 1(a) with truncation.

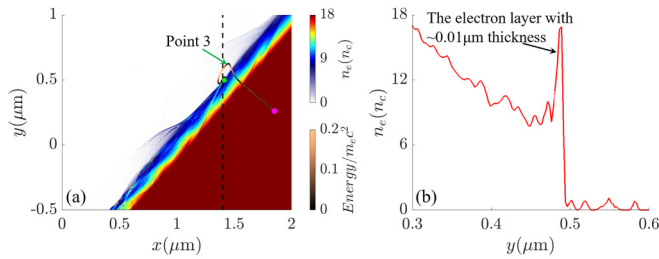


FIG. 9. (a) Typical trajectory of the electrons' motion in the laser preplasma interaction with truncation. The background color shows the distribution of the electron density n_e at $t = 8.25T_0$. (b) The distribution of the electron density n_e at $x = 1.4 \mu\text{m}$ [the dashed black line in panel (a)].

like a solitary wave, successively producing XUV and x-ray radiation every time its experienced laser magnetic field changes its direction. Although the kinetic energy of a characteristic electron is low and usually below $\sim m_e c^2$, the number of such electrons is massive. So they can irradiate strong radiation at frequencies beyond the limitation of the power law. For the effects of the plasma density, a profile with a truncation beyond the critical point is used. The radiation

order can only reach $n \approx 20$ th, much lower than $n = 100$ th in the case without the density profile truncation. This is because the electron layer cannot be compressed as thin as a nanometer and the kinetic energy obtained from the laser is lower as the over-critical density at the profile truncation point prevents effective acceleration of electrons. With the development and improvement of few-cycle laser technology, it is a prospective method to realize the generation of “water window” radiation effectively in the laser-solid plasma interaction.

ACKNOWLEDGMENTS

This project was supported by the Young Scientists Fund of the National Natural Science Foundation of China (Grant No. 12204131), the Strategic Priority Research Program of the Chinese Academy of Sciences, China (Grants No. XDA25030300 and No. XDA25010100), and the Natural Science Foundation of Shandong Province (Grant No. ZR2019ZD44). The authors appreciate all the anonymous referees who provided very constructive suggestions to improve our studies.

- [1] D. Popmintchev, B. R. Galloway, M.-C. Chen, F. Dollar, C. A. Mancuso, A. Hankla, L. Miaja-Avila, G. O'Neil, J. M. Shaw, G. Fan *et al.*, *Phys. Rev. Lett.* **120**, 093002 (2018).
- [2] G. Lambert, T. Hara, D. Garzella, T. Tanikawa, M. Labat, B. Carre, H. Kitamura, T. Shintake, M. Bougeard, S. Inoue *et al.*, *Nat. Phys.* **4**, 296 (2008).
- [3] A. Ravasio, D. Gauthier, F. R. N. C. Maia, M. Billon, J.-P. Caumes, D. Garzella, M. Géléoc, O. Gobert, J.-F. Hergott, A.-M. Pena *et al.*, *Phys. Rev. Lett.* **103**, 028104 (2009).
- [4] J. L. Krause, K. J. Schafer, and K. C. Kulander, *Phys. Rev. Lett.* **68**, 3535 (1992).
- [5] C. Liu, P. Wei, J. Miao, C. Zhang, Y. Huang, Y. Zheng, Y. Leng, and Z. Zeng, *Chin. Opt. Lett.* **12**, 030201 (2014).
- [6] J. Jiang, P. Wei, Z. Zeng, X. Yuan, Y. Zheng, X. Ge, R. Li, and Z. Xu, *Chin. Opt. Lett.* **13**, 050202 (2015).
- [7] U. Teubner and P. Gibbon, *Rev. Mod. Phys.* **81**, 445 (2009).
- [8] F. Krausz and M. Ivanov, *Rev. Mod. Phys.* **81**, 163 (2009).
- [9] S. X. Hu and L. A. Collins, *Phys. Rev. Lett.* **96**, 073004 (2006).
- [10] F. Quéré, C. Thauray, P. Monot, S. Dobosz, Ph. Martin, J.-P. Geindre, and P. Audebert, *Phys. Rev. Lett.* **96**, 125004 (2006).
- [11] C. Thauray, F. Quéré, J.-P. Geindre, A. Levy, T. Ceccotti, P. Monot, M. Bougeard, F. Réau, P. d'Oliveira, P. Audebert *et al.*, *Nat. Phys.* **3**, 424 (2007).
- [12] P. Gibbon, *Phys. Rev. Lett.* **76**, 50 (1996).
- [13] T. Baeva, S. Gordienko, and A. Pukhov, *Phys. Rev. E* **74**, 046404 (2006).
- [14] B. Dromey, S. Rykovanov, M. Yeung, R. Hörlein, D. Jung, D. C. Gautier, T. Dzelzainis, D. Kiefer, S. Palaniyappan, R. Shah *et al.*, *Nat. Phys.* **8**, 804 (2012).
- [15] D. an der Brügge and A. Pukhov, *Phys. Plasmas* **17**, 033110 (2010).
- [16] J. Gao, F. Liu, X. L. Ge, Y. Q. Deng, G. B. Zhang, Y. Fang, W. Q. Wei, S. Yang, X. H. Yuan, M. Chen *et al.*, *Chin. Opt. Lett.* **15**, 081902 (2017).
- [17] M. Yeung, S. Rykovanov, J. Bierbach, L. Li, E. Eckner, S. Kuschel, A. Woldegeorgis, C. Rödel, A. Sävert, G. G. Paulus *et al.*, *Nat. Photonics* **11**, 32 (2017).
- [18] Z.-Y. Chen and A. Pukhov, *Nat. Commun.* **7**, 12515 (2016).
- [19] M. Cerchez, A. L. Giesecke, C. Peth, M. Toncian, B. Albertazzi, J. Fuchs, O. Willi, and T. Toncian, *Phys. Rev. Lett.* **110**, 065003 (2013).
- [20] A. Leblanc, S. Monchocé, C. Bourassin-Bouchet, S. Kahaly, and F. Quéré, *Nat. Phys.* **12**, 301 (2016).
- [21] G. Zhang, M. Chen, F. Liu, X. Yuan, S. Weng, J. Zheng, Y. Ma, F. Shao, Z. Sheng, and J. Zhang, *Opt. Express* **25**, 23567 (2017).
- [22] L. Chopineau, A. Denoëud, A. Leblanc, E. Porat, P. Martin, H. Vincenti, and F. Quéré, *Nat. Phys.* **17**, 968 (2021).
- [23] J. Gao, B. Li, F. Liu, Z.-Y. Chen, M. Chen, X. Ge, X. Yuan, L. Chen, Z. Sheng, and J. Zhang, *Phys. Rev. E* **101**, 033202 (2020).
- [24] G. Cantono, L. Fedeli, A. Sgattoni, A. Denoëud, L. Chopineau, F. Réau, T. Ceccotti, and A. Macchi, *Phys. Rev. Lett.* **120**, 264803 (2018).
- [25] J. Gao, B. Y. Li, F. Liu, H. P. Cai, M. Chen, X. H. Yuan, X. L. Ge, L. M. Chen, Z. M. Sheng, and J. Zhang, *Phys. Plasmas* **26**, 103102 (2019).
- [26] M. Bocoum, M. Thévenet, F. Böhle, B. Beaurepaire, A. Vernier, A. Jullien, J. Faure, and R. Lopez-Martens, *Phys. Rev. Lett.* **116**, 185001 (2016).
- [27] B. Y. Li, F. Liu, M. Chen, Z. Y. Chen, X. H. Yuan, S. M. Weng, T. Jin, S. G. Rykovanov, J. W. Wang, Z. M. Sheng, and J. Zhang, *Phys. Rev. E* **100**, 053207 (2019).
- [28] B. Y. Li, F. Liu, M. Chen, F. Y. Wu, J. W. Wang, L. Lu, J. L. Li, X. L. Ge, X. H. Yuan, W. C. Yan, L. M. Chen, Z. M. Sheng, and J. Zhang, *Phys. Rev. Lett.* **128**, 244801 (2022).
- [29] F. Dollar, P. Cummings, V. Chvykov, L. Willingale, M. Vargas, V. Yanovsky, C. Zwick, A. Maksimchuk, A. G. R. Thomas, and K. Krushelnick, *Phys. Rev. Lett.* **110**, 175002 (2013).

- [30] C. Thaury and F. Quéré, *J. Phys. B: At., Mol. Opt. Phys.* **43**, 213001 (2010).
- [31] A. Gonoskov, *Phys. Plasmas* **25**, 013108 (2018).
- [32] D. Herrmann, L. Veisz, R. Tautz, F. Tavella, K. Schmid, V. Pervak, and F. Krausz, *Opt. Lett.* **34**, 2459 (2009).
- [33] F. Tavella, Y. Nomura, L. Veisz, V. Pervak, A. Marcinkevčius, and F. Krausz, *Opt. Lett.* **32**, 2227 (2007).
- [34] K. Schmid, L. Veisz, F. Tavella, S. Benavides, R. Tautz, D. Herrmann, A. Buck, B. Hidding, A. Marcinkevicius, U. Schramm *et al.*, *Phys. Rev. Lett.* **102**, 124801 (2009).
- [35] G. J. Ma, W. Dallari, A. Borot, F. Krausz, W. Yu, G. D. Tsakiris, and L. Veisz, *Phys. Plasmas* **22**, 033105 (2015).
- [36] J. J. Carrera, X. M. Tong, and S. Chu, *Phys. Rev. A* **74**, 023404 (2006).
- [37] Y. Pertot, C. Schmidt, M. Matthews, A. Chauvet, M. Huppert, V. Svoboda, A. Conta, A. Tehlar, D. Baykusheva, J.-P. Wolf *et al.*, *Science* **355**, 264 (2017).
- [38] M. Cherednychek and A. Pukhov, *Phys. Plasmas* **23**, 103301 (2016).
- [39] N. M. Fasano, M. R. Edwards, and J. M. Mikhailova, *Phys. Plasmas* **30**, 063904 (2023).
- [40] M. Shirozhan, M. Moshkelgosha, and R. Sadighi-Bonabi, *Laser Part. Beams* **32**, 285 (2014).
- [41] M. R. Edwards, N. M. Fasano, and J. M. Mikhailova, *Phys. Rev. Lett.* **124**, 185004 (2020).
- [42] T. G. Blackburn, A. A. Gonoskov, and M. Marklund, *Phys. Rev. A* **98**, 023421 (2018).
- [43] S. Bhadoria, T. Blackburn, A. Gonoskov, and M. Marklund, *Phys. Plasmas* **29**, 093109 (2022).
- [44] R. A. Fonseca, L. O. Silva, F. S. Tsung, V. K. Decyk, W. Lu, C. Ren, W. B. Mori, S. Deng, S. Lee, T. Katsouleas, and J. C. Adam, *Lect. Notes Comput. Sci.* **2331**, 342 (2002).
- [45] G. Blaclard, H. Vincenti, R. Lehe, and J. L. Vay, *Phys. Rev. E* **96**, 033305 (2017).
- [46] Z. Chang, A. Rundquist, H. Wang, M. M. Murnane, and H. C. Kapteyn, *Phys. Rev. Lett.* **79**, 2967 (1997).
- [47] Ch. Spielmann, N. H. Burnett, S. Sartania, R. Koppitsch, M. Schnürer, C. Kan, M. Lenzner, P. Wobrauschek, and F. Krausz, *Science* **278**, 661 (1997).
- [48] M. Schnürer, Ch. Spielmann, P. Wobrauschek, C. Strelt, N. H. Burnett, C. Kan, K. Ferencz, R. Koppitsch, Z. Cheng, T. Brabec, and F. Krausz, *Phys. Rev. Lett.* **80**, 3236 (1998).